Published in final edited form as:

Nat Nanotechnol. 2019 May ; 14(5): 420–425. doi:10.1038/s41565-019-0395-0.

Bright sub-20-nm cathodoluminescent nanoprobes for electron microscopy.

Maxim B. Prigozhin[#,1], **Peter C. Maurer**[#,1], **Alexandra M. Courtis**[2], **Nian Liu**[3,4], **Michael D. Wisser**[3], **Chris Siefe**[3], **Bining Tian**[5], **Emory Chan**[5], **Guosheng Song**[6,7], **Stefan Fischer**[3], **Shaul Aloni**[5], **D. Frank Ogletree**[5], **Edward S. Barnard**[5], **Lydia-Marie Joubert**[8,9], **Jianghong Rao**[6], **A. Paul Alivisatos**[2,10,11,12], **Roger M. Macfarlane**[13], **Bruce E. Cohen**[5], **Yi Cui**[3], **Jennifer A. Dionne**[3], **Steven Chu**[1,14,*]

[1]Department of Physics, Stanford University, Stanford, California 94305, United States

[2]Department of Chemistry, University of California at Berkeley, Berkeley, California 94720, United States

[3]Department of Materials Science and Engineering, Stanford University, Stanford, California 94305, United States

[4]Current address: School of Chemical and Biomolecular Engineering, Georgia Institute of Technology, Atlanta, Georgia 30332, United States

[5]Molecular Foundry, Lawrence Berkeley National Laboratory, Berkeley, California 94720, United States

[6]Department of Radiology, Stanford University, Stanford, California 94305, United States

[7]Current address: State Key Laboratory of Chemo/Biosensing & Chemometrics, College of Chemistry & Chemical Engineering, Hunan University, Changsha 410082, China

[8]CSIF Beckman Center, Stanford University, Stanford, California 94305, United States

[9]Current address: EM Unit, Central Analytical Facilities, Stellenbosch University, South Africa

[10]Materials Sciences Division, Lawrence Berkeley National Laboratory, Berkeley, California 94720, United States

[*]schu@stanford.edu.

[#]These authors contributed equally to this work.

Author contributions

M.B.P., P.C.M., and S.C. conceived the project, designed experiments, analyzed the data, and interpreted the results. M.B.P. and P.C.M. conducted CL imaging experiments and wrote software for data analysis. M.B.P., P.C.M., A.M.C., N.L., M.D.W., C.S., B.T., G.S., and S.F. synthesized and characterized rare-earth nanoparticles. E.C. provided software for the simulation of the nanoparticle spectra. S.A., D.F.O., E.B., and L.-M.J. provided assistance and expertise in EM hardware and sample preparation. D.F.O. and S.A. developed the CL optics, and E.S.B. and D.F.O. developed the CL software. S.C. supervised research. J.R., A.P.A., R.M.M., B.E.C., Y.C., and J.A.D. supervised the relevant portions of the research such as sample preparation and training M.B.P. and P.C.M. on the nanoparticle synthesis. M.B.P., P.C.M., and S.C. wrote the manuscript.

Data availability. The datasets generated during and/or analyzed during the current study are available from the corresponding author on reasonable request.

Additional Information. Supplementary information is available in the online version of the paper. Reprints and permission information is available online at www.nature.com/reprints. Correspondence and requests for materials should be addressed to S.C.

Competing interests statement

The authors declare no conflict of interests.

[11.]Department of Materials Science and Engineering, University of California, Berkeley, California 94720, United States

[12.]Kavli Energy NanoScience Institute, Berkeley, California 94720, United States

[13.]IBM Research-Almaden, San Jose, California 95120, United States

[14.]Department of Molecular and Cellular Physiology, Stanford University, Stanford, California 94305, United States

Abstract

Electron microscopy (EM) has been instrumental in our understanding of complex biological systems. Although EM reveals cellular morphology with nanoscale resolution, it does not provide information on the location of different types of proteins. An EM-based bioimaging technology capable of localizing individual proteins and resolving protein-protein interactions with respect to cellular ultrastructure would provide important insights into the molecular biology of a cell. Here, we synthesized small lanthanide-doped nanoparticles, and measured the absolute photon emission rate of individual nanoparticles resulting from a given electron excitation flux (cathodoluminescence). Our results suggest that the optimization of nanoparticle composition, synthesis protocols and electron imaging conditions can lead to sub-20-nm nano-labels that would enable high signal-to-noise localization of individual biomolecules within a cellular context. In ensemble measurements, these labels exhibit narrow spectra of nine distinct colors, so that the imaging of biomolecules in a multicolor EM modality may be possible.

Nanoscale imaging of biomolecules in the context of cellular structures is essential to understand how cells function. Although conventional EM is a powerful tool for the study of heavy-metal-stained cellular ultrastructure (*i.e.* lipid membranes, cytoskeleton, chromatin, *etc.*), it does not implicitly provide information about the location of specific biomolecules. Several approaches have been developed to visualize proteins in an EM-micrograph, most notably tagging of target molecules with gold nanoparticles[1] and genetically encodable tags[2,3]. However, these electron-contrast-based techniques are inherently limited to imaging one protein species at a time, which prevents studying protein-protein interactions and other complex processes. A related technology based on photo-precipitation of lanthanide ion complexes and energy-filtered transmission electron microscopy (TEM) has been reported[4]. However, this technology does not have single-molecule sensitivity and requires a distinctly addressable photosensitizer molecule for each lanthanide ion color. In contrast, when EM is combined with optical super-resolution microscopy, different proteins can be tagged with spectrally distinguishable labels[5]. Although promising, such correlative light and EM methods require challenging sample preparation, suffer from systematic errors due to sample disruption at the nanoscale[5], and are susceptible to background luminescence[6].

An alternative approach to visualizing multiple proteins in an electron micrograph relies on tagging proteins with fluorescent molecules or nanoparticles, which, under excitation by an electron beam, emit light in a process known as cathodoluminescence (CL). In principle, this method allows for a simultaneous acquisition of an electron micrograph and the locations of different proteins. However, organic dyes and fluorescent proteins rapidly disintegrate under

electron exposure[7,8], and quantum dots are susceptible to bleaching in CL imaging[8]. Luminescent nanodiamonds and lanthanide-doped nanoparticles are more stable under electron beam irradiation and have been used for CL imaging, but only nanoparticles larger than ~40 nm[9–11] or large aggregates have been reported to show detectable CL signal[11]. The large size of these nanoparticles prevents specific protein labeling, which imposes a severe limitation on the use of these nanoparticles in biological experiments. In addition, a large fraction of the rare earth crystals were found to have aggregated into clusters of nanoparticles. [12,13] Even if such large nanoparticles can be synthesized so as not to form clusters, their size would not allow precise localization of the protein of interest with nanoscale resolution in an electron micrograph.

So far, it has remained an open question whether ‘bright’ cathodoluminescent nanoparticles can be synthesized on a sub-20nm size, which would be small enough to potentially enable protein labeling in biological systems. Here, we report on the development of cathodoluminescent lanthanide-doped $NaGdF_4$ nanocrystals with TEM nanoparticle full-width-half-maximum (FWHM) of 13.9 ± 5.0 nm (Fig. 1b and Fig. S4, and Fig. S5). The size of the developed nanoprobes is comparable to that of quantum dots, gold nanoparticles, and immunoglobulin antibodies, which are routinely used for immuno-labeling in EM[14,15].

In the work described here, a scanning electron microscope (SEM) with a parabolic reflector is used to excite the CL of lanthanide-doped nanoparticles and image the CL signal onto a photo-multiplying detector[16] (Methods section). In parallel with CL excitation and detection, the microscope also acquires the secondary electron (SE) signal from the same pixels that are registered in the CL channel (Fig. 1a). A key feature of CL imaging is its inherent nanoscale resolution. An electron beam with an energy of a few kiloelectron volts (keV) can be focused down to a few nanometers, although the resolution is usually limited by other factors such as CL excitation volume (Supplementary Information section “Measurements and analysis of the electron beam sample interaction volume”), nanoparticle size, and nanoparticle surface functionalization.

As an example of the capability of CL microscopy, a CL-SEM image of a single $NaGdF_4$:5% Eu^{3+} nanoparticle was acquired detecting both the SE and the CL signal in parallel (Fig. 1c). Cross-sectional line profiles of the SE (red) and CL (blue) signals from the same nanoparticle suggest that both EM and CL imaging can have comparable resolution typical of SEM. In contrast, a confocal optical scan of an upconverting lanthanide-doped nanoparticle ($NaYF_4$: 18% Yb^{3+}, 2% Er^{3+}) of a similar size shows a diffraction-limited point spread function typical of optical far field confocal microscopy. The specific nanoparticle shown in Fig. 1c was taken from a representative sample (see green star in Fig. 3b and green data point in Fig. 3d).

Previous work on lanthanide-doped nanoparticle synthesis has mainly been focused on obtaining nanoparticle compositions that optimize excitation and emission efficiency in optical upconversion[17], a process which is fundamentally different from CL excitation[18]. Therefore, an independent investigation of the CL brightness of rare-earth nanoparticles as a function of their composition was required. Such optimization was achieved by synthesizing a series of $NaGdF_4$ and $NaYF_4$ nanoparticles of varying Eu^{3+} doping levels (Methods) and

characterizing their CL brightness at the single-nanoparticle level (Methods). Nanoparticles were synthesized using a colloidal synthesis method as described in the Methods[19–22] (Supplementary Information Fig.S1-S3). The as-synthesized nanoparticles were ligand-exchanged with nitrosonium tetrafluoroborate ($NOBF_4$) and dispersed in dimethylformamide (DMF) (Methods)[23]. For CL-SEM imaging, multiple samples from the same synthesis run were prepared by spin-coating the dispersion of nanoparticles in DMF on a silicon substrate. The concentration of the nanoparticle solution used for spin-coating was adjusted so that at least three isolated nanoparticles could be found in an area of 1 μm^2. The samples were imaged in CL-SEM as described in the Methods.

Figure 2a-b shows a sample CL-SEM image of $NaGdF_4$:5% Eu^{3+} nanoparticles (Fig. 3b (magenta arrow), and Fig. 3d (magenta point)). In a typical experiment, a 1 μm^2 field of view was imaged with a 1.95 nm pixel pitch (comparable to the typical electron beam size) and a pixel dwell time of 2 ms using a 5 keV electron beam with a current of ~400 pA (current density ~100 pA/nm^2; ~6.2 x 10^6 electrons s^{-1} $Å^{-2}$; dose is ~12.5 x 10^3 electrons $Å^{-2}$ within the 2 ms pixel dwell time). The SE image (Fig. 2a) was collected in parallel with the CL image (Fig. 2b). In order to extract the CL intensity and CL signal-to-noise ratio (CL SNR) for individual nanoparticles, a sub-region within the original 1 μm^2 field of view containing one or several individual nanoparticles was selected. Nanoparticle aggregates were deliberately excluded from the analysis. For the case when a single nanoparticle was selected, its raw image was fitted to a two-dimensional Gaussian function with a linearly sloped background. This fit was used to extract the CL intensity and the signal-to-noise ratio for each individual nanoparticle (Methods). To compute the CL SNR, the CL signal was assumed to follow a Poisson distribution. This assumption was based on the analysis of the background from repeated SEM-CL scans (See SI section “Background CL noise is described by Poisson statistics” and Fig. S10). Because the ions that comprise rare-earth nanoparticles have high atomic numbers compared to the constituents of the biological tissue, a positive identification of a nanoparticle can be done using the SE or back-scattered electron signal. In this work, every $NaGdF_4$:5% Eu^{3+} nanoparticle was clearly seen on the Si substrate in the SE detection channel. Once a nanoparticle is identified in the electron imaging channel, CL counts are only required to identify the spectral identity of this nanoparticle, which relaxes the signal-to-noise ratio requirements. (For further details, see Methods and Supplementary Information section “Single-particle signal-to-noise ratio,” Fig. S13 and “Estimation of the number of observable colors and the required photon count rate”). However, as described in the sections “Single-particle signal-to-noise ratio” and “CL noise scaling of individual nanoparticles”, the actual “noise”, as it is defined in this section, can be larger by up to a factor of 2 due to systematic effects such as astigmatism,, charging, and drift (see Supplementary Information section “CL noise scaling of individual nanoparticles” and Fig. S11). Because of these effects, we conservatively define an individual nanoparticle to be observable in the CL channel if the CL SNR of this nanoparticle is greater than 10, instead of the CL SNR of ~2 that would be sufficient if the noise was purely Poissonian.

The pixel pitch of 1.95 nm is significantly smaller than the SEM nanoparticle FWHM of 21 ± 6 nm (Fig. 2d; 13.9 ± 5.0 nm TEM FWHM; see SI Fig. S4 and Fig. S5), leading to oversampling. An improvement in signal quality can be achieved through Fourier filtering.

Fig. 2c-e shows the CL intensity after Gaussian-filtering the image. In Fig. 2d, the CL counts per second and the CL SNR of all the individual nanoparticles from Fig. 2a,b are shown. CL intensity data in Fig. 2d are fit to a cubic curve (volumetric scaling, $FWHM^3$, see blue curve), and CL SNR data are fit to an exponent of 3/2 (square root scaling of the noise with respect to the signal, see red curve). The deviation of the data from the cubic fit indicates that the intensity does not follow a simple volumetric dependence with the SEM nanoparticle FWHM, in accordance with surface quenching reported for small optically excited nanoparticles[24]. Importantly, Fig. 2d illustrates that 13.9 ± 5.0 nm TEM FWHM nanoparticles can be observed in CL microscopy. Fig. 2f,g depicts three-dimensional visualizations of the CL signal of individual nanoparticles highlighted with red and yellow boxes in Fig. 2c, respectively. The data points for the nanoparticles in Fig. 2f are highlighted in Fig. 2d with diamonds (CL signal, left axis) and circles (CL SNR, right axis). The corresponding SEM scan in Fig. 2a proves that the CL emission originates from individual nanoparticles. For example, the dimmer particle in the red rectangle in Fig. 2c has a CL SNR of 15.7 and is clearly visible in the filtered CL image (Fig. 2f).

Despite high CL intensity in certain samples, the CL emission of $NaGdF_4:Eu^{3+}$ nanoparticles varied drastically between different experiments. Even on a single sample (*i.e.* a single 5 x 5 mm Si wafer substrate), the CL signal fluctuated as a function of the imaging position (Fig. 3a, and SI Figs. S16-S22). Similar sample preparation also resulted in a large variation in signal, even if these samples were prepared from the same nanoparticle stock solution (Fig. 3b). Finally, particles that were synthesized under nominally identical conditions resulted in dramatically different CL emission rates (Fig. 3c). In the field of view (1 μm^2) that contains the nanoparticles with the largest CL emission rate (Position 5 in Fig. 3a, SI Fig. S21) an average CL signal of (7.1 ± 2.2) x 10^5 counts/s was observed, but in other cases (*e.g.* Position 7 in Fig. 3a, SI Fig. S23) the nanoparticles imaged by the CL-SEM were barely detectable in the CL channel. Table S1 in the Supplementary Information tabulates the number of SEM detected particles, and the number and fraction of nanoparticles with CL SNR>10. The high variability of the CL signal for $NaGdF_4:Eu^{3+}$ nanoparticles may originate from material-specific or synthesis-specific defects that lead to quenching of the luminescence. Such quenching can be caused, for example, by electron beam damage of the surrounding organic material or the nanoparticle itself[25]. CL brightness of $NaGdF_4$ nanoparticles as a function of Eu^{3+} doping level was also investigated (Fig. 3d). $NaGdF_4$ doped with Er^{3+} at various doping levels showed no detectable CL luminescence at the single-nanoparticle level (Fig. S24a). Notably, the large variability in the CL brightness of individual $NaGdF_4:Eu^{3+}$ nanoparticles was masked in ensemble CL measurements (Fig. S26). This observation highlights the importance of single-nanoparticle CL measurements. In addition, CL brightness of ~35 nm SEM FWHM $NaYF_4$ nanoparticles (Fig. S6 and S7) doped with Eu^{3+} (Fig. S25) and with Er^{3+} (Fig. S24b) was more consistent from sample to sample as compared to the $NaGdF_4$ nanoparticles. Further CL nanoprobe development is needed to achieve sub-20-nm nanoparticles with consistently high CL luminescence required for biological cell imaging.

Lanthanide ions have rich energy level diagrams with 4*f*-to-4*f* transitions that give rise to emission spectra that are characteristic of each individual lanthanide ion. Fig. 4 shows ensemble CL spectra obtained for nine different types of $NaGdF_4$ nanoparticles doped with

Eu^{3+}, Er^{3+}, Ho^{3+}, Tb^{3+}, Sm^{3+}, Dy^{3+}, Nd^{3+}, Tm^{3+} and Yb^{3+} ions (see SI, Fig. S6 for TEM images of $NaYF_4$ nanoparticles and Fig. S27 for the CL spectra of $NaYF_4$ nanoparticles). The Er^{3+} doping was at 20 %, while all other lanthanide ions were doped at 15 %. All the spectra were acquired from films of *n*-hexane-washed nanoparticles using a JEOL JXA-8230 SuperProbe instrument (beam energy is 5 keV; probe current ~0.13 pA/nm^2, ~8 x 10^3 electrons s^{-1} Å^{-2}; see Methods). In addition, doping with Ce^{3+} and Pr^{3+}, and Gd^{3+} alone was investigated but did not yield sharp spectra (see SI, Fig. S30 for the spectra of Ce^{3+}, Pr^{3+}, and Gd^{3+}).

The narrow emission lines (21 ± 11 nm FWHM of spectral peaks) of lanthanide-doped nanoparticles and their invariance with respect to the host lattice are indicative of atom-like 4*f*-to-4*f* inner-shell transitions in lanthanide ions. The intensities of transitions among these low-lying 4*f* states in lanthanide ions can be qualitatively described by the Judd–Ofelt theory[26,27]. Fig. 4 compares the experimental spectra to Judd–Ofelt theory[26,27] (See SI section “Simulations of nanoparticle spectra”, Fig. S31). Differences in the oscillator strength of individual transitions likely arise because the Judd-Ofelt parameters often relied on rates extracted from different host lattices[28].

This work explores small sub-20 nm lanthanide-doped nanoparticles as prospective nanoscale labels for multicolor EM owing to their potentially high photon count rate, sharp emission spectra, and tunable size. The size of lanthanide-doped nanoparticles presented here is comparable to that of quantum dots that are commonly used as luminescent labels in optical imaging[15], and only slightly larger than gold nanoparticles used in EM[14]. This substantial reduction in nanoparticle size compared to the previously reported cathodoluminescent nanoparticles is a significant improvement because nanoparticles on the order of 10–20 nm in diameter are required for efficient biomolecular targeting and subsequent nanoscale localization of the molecules of interest in CL microscopy. A further reduction in size may be achieved by engineering core-shell structures that eliminate the adverse effects of the nanoparticle surface[29,30].

Furthermore, the long excited state lifetimes of rare-earth nanoparticles[31] enable time-gated measurements that eliminate CL background from the biological substrate[32] (Fig. S29) and would allow imaging even smaller nanoparticles that have a lower CL intensity but are more suitable for targeted protein labeling and penetration into tissue samples[13]. Although the focus of the work presented here is on the development of bright cathodoluminescent nanoparticles, the CL background from potential biological substrates needs to be taken into account when designing optimal CL nanoprobes. Background-free measurements would make the detection of a few photons sufficient to successfully assign the nanoparticle color (see SI section “Estimation of number of observable colors and required photon count rate”), potentially opening a path to ultra-small labels for multicolor biological electron microscopy.

A better signal-to-noise ratio could be achieved if the electron interaction volume is matched to the nanoparticle size (for a 15–20 nm diameter nanoparticle this corresponds to 0.75–1 keV electron landing energies, see SI section “Measurements and analysis of the electron beam sample interaction volume”). Theoretical analysis of inelastic scattering suggests that

for a 15–20 nm diameter nanoparticle, the electron interaction volume would match the nanoparticle dimensions at the electron landing energy of 0.75–1 keV (Fig. S16). In addition, this local excitation would also minimize the background from excitation by back-scattered and SE in the substrate (Fig. S14-15). Imaging energy of ~1 keV are also an optimal trade-off between the back-scattered electron contrast and the axial resolution in biological SEM[33]. In the future, rapid nanoparticle localization in the electron detection channel may allow addressing each identified nanoparticle individually and significantly reduce the image acquisition time and electron dosage. Combining CL microscopy with the new multi-beam SEMs is expected to further increase the imaging speed.

Finally, the next generation of our experiment will focus on the optimization of the synthesis parameters for the other lanthanide ions (*i.e.* Ho^{3+}, Tb^{3+}, Sm^{3+}, Dy^{3+}, Nd^{3+}, Tm^{3+} and Yb^{3+}). Such an optimization, combined with a new multicolor-CL imaging system, which enables a simultaneous detection of multiple spectral components, may open the door to true multicolor imaging at the single-nanoparticle level. The potentially large photon count rate of individual nanoparticles (*i.e.* $NaGdF_4$:5% Eu^{3+}) combined with the distinct spectra obtained in ensemble measurements suggest that up to nine different colors with 10–20 nm spatial resolution could potentially be achieved (See SI section “Estimation of the number of observable colors and the required photon count rate”, Fig. S28)[34]. A further increase in the number of colors may be achieved by co-doping nanoparticles with multiple lanthanide ions and detecting an emission spectrum characteristic of the exact particle composition[28]. Incidentally, another benefit of using low beam energy in CL imaging lies in the imaging of several nanoprobes of different colors because the spectral identification would be compromised if stray electrons were able to excite neighboring nanoparticles (See SI section “Measurements and analysis of the electron beam sample interaction volume”).

Although reliable multicolor CL imaging at the single-nanoparticle level and in biological tissue remains to be demonstrated, our findings motivate future work in this direction. Optimal multicolor imaging combined with advances in particle functionalization and labeling[35] could allow visualizing the locations of different proteins with respect to the cellular ultrastructure (*i.e.* organelles, vesicles, nucleic acids, and other nanostructures). Protein-specific localization in the context of ~5 nanometer cell ultrastructure could have a and so significant impact our understanding of the molecular architecture of the cell. Likewise, combining multicolor CL imaging with *in situ* serial-block-face SEM[36] or focused ion beam SEM[37] will permit full three-dimensional reconstruction of entire tissue sections[37,38], while providing simultaneous nanoscale protein localization. Such bio-specific volumetric electron imaging would enable the visualization of different cell types within heterogeneous tissue sections and shed light onto the organization of complex systems such as the heart[39], the brain[38], or cancerous tissue[40].

Methods

Nanoparticle synthesis and characterization.

A series of nanoparticles was synthesized including $NaGdF_4$:Eu^{3+} and $NaGdF_4$:Er^{3+} doped at 0, 2, 5, 10, 20, 30, 50, 80, and 100 %; $NaYF_4$:Eu^{3+} doped at 2, 5, 10, and 20 %; $NaYF_4$:Er^{3+} doped at 5, 10, and 30 %; $NaGdF_4$ nanoparticles doped with Ho^{3+}, Tb^{3+}, Sm^{3+},

Dy^{3+}, Nd^{3+}, Tm^{3+}, Ce^{3+}, Pr^{3+}, and Yb^{3+} at 15 %; and $NaYF_4$ nanoparticles doped with Ho^{3+}, Tb^{3+}, Sm^{3+}, Dy^{3+}, Nd^{3+}, Tm^{3+}, Ce^{3+}, Pr^{3+}, and Yb^{3+} at 5 %. Synthesis was based on the previously reported protocols[19–22] (see SI section "Nanoparticle synthesis and characterization" for details). Briefly, 4 mL of oleic acid and 6 mL of 1-octadecene were mixed with 0.4 mL total volume (0.4 mmol) of an aqueous solution of 1 M rare-earth (RE) chloride hydrates of desired ratios. The temperature was set to 110 °C for 40 minutes. Afterwards, the solution was cooled to <30 °C. Next, a nucleation precursor solution was prepared by adding 1 mL of 1 M sodium hydroxide in methanol to 4 mL of 0.4 M ammonium fluoride in methanol. After mixing, the precursor solution was vortexed for 10 s and injected into the RE-oleate mixture at room temperature under argon atmosphere. The temperature was maintained at 50 °C under argon atmosphere for 40 minutes. The temperature was further increased to 80 °C and the reaction was either exposed to air or put under vacuum allowing methanol to evaporate. The temperature was stabilized at 100 °C for 15 min under vacuum. Afterwards, the reaction was placed under argon atmosphere and the temperature was increased to 300 °C ($NaYF_4$) or 320 °C ($NaGdF_4$) at a mean rate of ~15 °C/min. The growth temperature was maintained for 60 ($NaGdF_4$) or 90 ($NaYF_4$) minutes before cooling the reaction to <30 °C. The samples were stored as-synthesized in oleic acid 1-octadecene. Nanoparticle characterization was done using TEM (Fig. S4-S7) and inductively coupled plasma mass spectrometry (Fig. S8 and S26).

Sample preparation for single-nanoparticle CL measurements.

The nanoparticles were exchanged into dimethylformamide (DMF) using a modification of a published procedure[23] (see SI section "Single-particle CL sample preparation" and Fig. S9 for details). Briefly, 0.5–1 mL of as-synthesized nanoparticles were mixed with an equal volume of ethanol and washed by centrifugation at 3,500 g for 3 minutes. The pellet was resuspended with 0.5 mL *n*-hexane and the 0.5 mL ethanol wash was repeated. The pellet was then resuspended in 0.3 mL of *n*-hexane, 0.3 mL of 11 mg/mL nitrosonium tetrafluoroborate ($NOBF_4$) in DMF was added, and the reaction was incubated for 45 minutes. The tube was centrifuged at 10,000 g for 10 minutes and the supernatant was discarded. The pellet was washed with 0.2 mL of a 1:1 mixture of toluene and *n*-hexane at 10,000 g for 10 minutes. The resulting nanoparticle pellet was dried under argon and resuspended in 0.1–0.2 mL of DMF. 4 μL of nanoparticles in DMF were spin-coated on a silicon substrate to achieve a density compatible with imaging several single nanoparticles within a 1 μm^2 region.

Single-nanoparticle CL measurements.

Single-nanoparticle CL measurements were done at the Molecular Foundry at the Lawrence Berkeley National Laboratory. Experiments were performed on a Zeiss Supra 55-VP-FESEM with a CL parabolic mirror light collection system. A 1.3π sr (1 mm focal length) diamond-turned aluminum parabolic reflector mounted on a 4-axis nanopositioning stage was used to collimate the light emitted from the sample. The light was then focused onto a photomultiplier counting module (Hamamatsu H7442–40). During the measurements, the working distance was typically in the 4.9–5.2 mm range, the current was on the order of 300–500 pA, and the beam energy was 5 keV. The samples were scanned using a 512 x 512 point grid of 1 μm x 1 μm dimensions resulting in a pixel pitch of 1.95 nm. The dwell time

per pixel was either 500 μs or 2 ms depending on the experiment and expected count rates. The estimated electron dose under these conditions was approximately 5,000–20,000 electrons/Å^2 (current density ~100 pA/nm^2).

Single-nanoparticle CL data analysis.

The CL intensity and signal-to-noise ratio for individual nanoparticles is extracted by selecting a sub-region (approx. 30 x 30 pixels, or ~7–8 σ for $NaGdF_4$:Eu^{3+}) within the original 1 μm^2 field of view, which contains one or several individual particles. Nanoparticle aggregates were avoided. The raw CL image $I(x_i, y_i)$, where x_i and y_i are discrete pixels of 1.95 nm pitch and I is measured in counts per pixel, was then fitted by a two-dimensional Gaussian function with a linearly sloped background of the form $G(x_i, y_i) = c_o + c_1 y_i + c_2 x_i + Ae^{\frac{-(x_i - x_o)^2 - (y_i - y_o)^2}{2\sigma^2}}$ (Fig. S12). In the fit routine the starting parameters for the standard deviation σ and the center x_0 and y_0 positions were obtained from similar fits to the SE signal. The standard deviation of the CL image was constrained to not deviate by more than 10 % from the SE image. The Gaussian component of the fitted function $S(x_i, y_i) = Ae^{\frac{-(x_i - x_o)^2 - (y_i - y_o)^2}{2\sigma^2}}$ represents the CL signal of an individual nanoparticle. The sum of $S(x_i, y_i)$ corresponds to the number of counts associated with each nanoparticle. Note, since the "counts" are derived from a fitted function, the sum is generally not an integer. The signal-to-noise ratio was calculated by first summing up the CL signal of the nanoparticle $S_{total} = \sum_i S(x_i, y_i)$ including only the pixels in which the signal is greater than a defined threshold, which is commonly taken as the signal at pixels 2σ (95% confidence level) away from the center of the Gaussian distribution. The threshold of 2σ was used because it is ideal when the background level is equal to the amplitude of the Gaussian of the fitted CL signal, which is the case for the data collected in this work. The noise was calculated for the same pixels as $N_i = \sqrt{G(x_i, y_i)}$ and the total noise was determined by adding the noise for each pixel in quadrature:$N_{total} = \sqrt{\sum_i N_i^2}$. The overall signal-to-noise ratio for a single nanoparticle was then defined as the ratio $SNR = \frac{S_{total}}{N_{total}}$. The nanoparticle SEM full-width-half-maximum (FWHM) was calculated from the standard deviation, as nanoparticle SEM FWHM = $2\sigma\sqrt{2\ln 2} = 2.35\sigma$. Note that in this analysis the CL signal is approximated by a Gaussian function, and does not include such imaging artifacts as astigmatism, sample drift, or charging.

Ensemble CL measurements.

0.5 mL of as-synthesized nanoparticle solution in oleic acid and 1-octadecene was washed three times with 0.5 mL ethanol at 3.5 g for 3 minutes at room temperature. The nanoparticles were redispersed in *n*-hexane and drop-cast repeatedly on a ~5 mm x 5 mm piece of silicon wafer until an opaque white film of nanoparticles was visible by eye. Nanoparticle spectra were measured with a JEOL JXA-8230 SuperProbe electron

microscope equipped with an xCLent III hyperspectral CL system. See SI section "Ensemble spectral measurements and sample preparation" for further details.

Simulations of nanoparticle spectra.

The luminescence spectra for different dopants (Eu^{3+}, Er^{3+}, Ho^{3+}, Tb^{3+}, Sm^{3+}, Dy^{3+}, Nd^{3+}, Tm^{3+} and Yb^{3+}) were qualitatively estimated by the Judd-Ofelt theory[26,27]. A rate-equation-based model, which incorporates electric and magnetic dipole transitions, cross relaxations between multiple rare-earth ions, and multi-phonon relaxations in the host lattice was used (for more details on the software package we refer to Chan *et al.*[28]). Although electron excitation generally involves high-lying energy states, which cannot be described by the Judd-Ofelt theory, emission in the visible spectrum can be accurately modeled. The present Judd-Ofelt simulations were restricted to energy levels below 25,000 cm^{-1}.

Supplementary Material

Refer to Web version on PubMed Central for supplementary material.

Acknowledgements

This work was supported by the Gordon and Betty Moore Foundation grant number 4309, and supported by the NIH grant 1R01GM128089–01A1. Work at the Molecular Foundry was supported by the Office of Science, Office of Basic Energy Sciences, of the U.S. Department of Energy under Contract No. DE-AC02–05CH11231. Part of this work was performed at the Stanford Nano Shared Facilities (SNSF), supported by the National Science Foundation under award ECCS-1542152. Access to the JEOL TEM 1400 was provided through the Stanford Microscopy Facility, NIH grant SIG number 1S10RR02678001. M.B.P. was supported by the Helen Hay Whitney Foundation Postdoctoral Fellowship, and P.C.M. was supported through the Stanford Neuroscience Interdisciplinary Award. M.D.W. and J.A.D. acknowledge financial support provided as part of the DOE "Light-Material Interactions in Energy Conversion" Energy Frontier Research Center under grant DE-SC0001293, as well as funding provided by the Global Climate and Energy Project at Stanford University. The authors thank Prof. Naomi Ginsberg and Dr. Clarice Aiello for providing software used in time-gated CL imaging experiments and for stimulating discussions. The authors are also grateful to Dr. John J. Perrino and Dr. Dale H. Burns for providing expertise in EM and for stimulating discussions. We thank Prof. Ronald Walsworth, Dr. David Glenn, and Dr. Huiliang Zhang; Prof. Thomas C. Sudhof and Dr. Justin Trotter; Dr. Joshua Collins; and Dr. Xianchuang Zheng for stimulating discussions.

References

1. Roth J, Bendayan M & Orci L Ultrastructural localization of intracellular antigens by the use of protein A-gold complex. J. Histochem. Cytochem. 26, 1074–1081 (1978). [PubMed: 366014]
2. Martell JD et al. Engineered ascorbate peroxidase as a genetically encoded reporter for electron microscopy. Nat. Biotechnol. 30, 1143–8 (2012). [PubMed: 23086203]
3. Lam SS et al. Directed evolution of APEX2 for electron microscopy and proximity labeling. Nat Methods 12, 51–54 (2015). [PubMed: 25419960]
4. Adams SR et al. Multicolor Electron Microscopy for Simultaneous Visualization of Multiple Molecular Species. Cell Chem. Biol. 23, 1417–1427 (2016). [PubMed: 27818300]
5. Sochacki K. a, Shtengel G, van Engelenburg SB, Hess HF & Taraska JW Correlative super-resolution fluorescence and metal-replica transmission electron microscopy. Nat. Methods 11, 305–8 (2014). [PubMed: 24464288]
6. Carter SD et al. Distinguishing signal from autofluorescence in cryogenic correlated light and electron microscopy of mammalian cells. J. Struct. Biol. 201, 15–25 (2018). [PubMed: 29078993]
7. Fisher PJ, Wessels WS, Dietz AB & Prendergast FG Enhanced biological cathodoluminescence. Opt. Commun. 281, 1901–1908 (2008).

8. Mahfoud Z et al. Cathodoluminescence in a scanning transmission electron microscope: A nanometer-scale counterpart of photoluminescence for the study of II-VI quantum dots. J. Phys. Chem. Lett. 4, 4090–4094 (2013).
9. Zhang H, Glenn DR, Schalek R, Lichtman JW & Walsworth RL Efficiency of Cathodoluminescence Emission by Nitrogen-Vacancy Color Centers in Nanodiamonds. Small 13, 1–9 (2017).
10. Glenn DR et al. Correlative light and electron microscopy using cathodoluminescence from nanoparticles with distinguishable colours. Sci. Rep. 2, 1–6 (2012).
11. Niioka H et al. Multicolor cathodoluminescence microscopy for biological imaging with nanophosphors. Appl. Phys. Express 4, 1–4 (2011).
12. Cai E et al. Stable Small Quantum Dots for Synaptic Receptor Tracking on Live Neurons. Angew. Chemie Int. Ed. 53, 12484–12488 (2014).
13. Yokota S Effect of particle size on labeling density for catalase in protein A-gold immunocytochemistry. J. Histochem. Cytochem. 36, 107–109 (1988). [PubMed: 3335766]
14. Kijanka M et al. A novel immuno-gold labeling protocol for nanobody-based detection of HER2 in breast cancer cells using immuno-electron microscopy. J. Struct. Biol. 199, 1–11 (2017). [PubMed: 28552722]
15. Giepmans BNG, Deerinck TJ, Smarr BL, Jones YZ & Ellisman MH Correlated light and electron microscopic imaging of multiple endogenous proteins using Quantum dots. Nat Methods 2, 743–749 (2005). [PubMed: 16179920]
16. Bischak CG et al. Cathodoluminescence-activated nanoimaging: Noninvasive near-field optical microscopy in an electron microscope. Nano Lett. 15, 3383–3390 (2015). [PubMed: 25855869]
17. Feng W, Zhu X & Li F Recent advances in the optimization and functionalization of upconversion nanomaterials for in vivo bioapplications. NPG Asia Mater. 5, e75–15 (2013).
18. García De Abajo FJ Optical excitations in electron microscopy. Rev. Mod. Phys. 82, 209–275 (2010).
19. Wang F, Deng R & Liu X Preparation of core-shell NaGdF4 nanoparticles doped with luminescent lanthanide ions to be used as upconversion-based probes. Nat. Protoc. 9, 1634–1644 (2014). [PubMed: 24922272]
20. Liu Q, Feng W, Yang T, Yi T & Li F Upconversion luminescence imaging of cells and small animals. Nat. Protoc. 8, 2033–2044 (2013). [PubMed: 24071909]
21. Li Z & Zhang Y An efficient and user-friendly method for the synthesis of hexagonal-phase NaYF4:Yb, Er/Tm nanocrystals with controllable shape and upconversion fluorescence. Nanotechnology 19, (2008).
22. Ostrowski AD et al. Controlled synthesis and single-particle imaging of bright, sub-10 nm lanthanide-doped upconverting nanocrystals. ACS Nano 6, 2686–2692 (2012). [PubMed: 22339653]
23. Dong A et al. A generalized ligand-exchange strategy enabling sequential surface functionalization of colloidal nanocrystals. J. Am. Chem. Soc. 133, 998–1006 (2011). [PubMed: 21175183]
24. Gargas DJ et al. Engineering bright sub-10-nm upconverting nanocrystals for single-molecule imaging. Nat. Nanotechnol. 9, 300–305 (2014). [PubMed: 24633523]
25. Feng W, Sun LD, Zhang YW & Yan CH Solid-to-hollow single-particle manipulation of a self-assembled luminescent NaYF4:Yb,Er nanocrystal monolayer by electron-beam lithography**. Small 5, 2057–2060 (2009). [PubMed: 19507152]
26. Judd BR Optical absorption intensities of rare-earth ions. Phys. Rev. 127, 750–761 (1962).
27. Ofelt GS Intensities of Crystal Spectra of Rare-Earth Ions. J. Chem. Phys. 37, 511–520 (1962).
28. Chan EM Combinatorial approaches for developing upconverting nanomaterials: High-throughput screening, modeling, and applications. Chem. Soc. Rev. 44, 1653–1679 (2015). [PubMed: 25287124]
29. Fischer S, Johnson NJJ, Pichaandi J, Goldschmidt JC & Van Veggel FCJM Upconverting core-shell nanocrystals with high quantum yield under low irradiance: On the role of isotropic and thick shells. J. Appl. Phys. 118, (2015).
30. Ma C et al. Optimal Sensitizer Concentration in Single Upconversion Nanocrystals. Nano Lett. 17, 2858–2864 (2017). [PubMed: 28437117]

31. Lu Y et al. Tunable lifetime multiplexing using luminescent nanocrystals. Nat. Photonics 8, 32–36 (2013).
32. Nawa Y et al. Dynamic autofluorescence imaging of intracellular components inside living cells using direct electron beam excitation. Biomed. Opt. Express 5, 378 (2014). [PubMed: 24575334]
33. Xu CS et al. Enhanced FIB-SEM systems for large-volume 3D imaging. Elife 3, 1–36 (2017).
34. Zhang Z, Kenny SJ, Hauser M, Li W & Xu K Ultrahigh-throughput resolved super-resolution microscopy. Nat Methods 12, 935–938 (2015). [PubMed: 26280329]
35. DaCosta MV, Doughan S, Han Y & Krull UJ Lanthanide upconversion nanoparticles and applications in bioassays and bioimaging: A review. Anal. Chim. Acta 832, 1–33 (2014). [PubMed: 24890691]
36. Denk W & Horstmann H Serial block-face scanning electron microscopy to reconstruct three-dimensional tissue nanostructure. PLoS Biol. 2, (2004).
37. Hayworth KJ et al. Ultrastructurally smooth thick partitioning and volume stitching for large-scale connectomics. Nat Methods 12, 319–322 (2015). [PubMed: 25686390]
38. Kasthuri N et al. Saturated Reconstruction of a Volume of Neocortex. Cell 162, 648–661 (2015). [PubMed: 26232230]
39. Stephenson RS et al. High resolution 3-Dimensional imaging of the human cardiac conduction system from microanatomy to mathematical modeling. Sci. Rep. 7, 1–13 (2017). [PubMed: 28127051]
40. Angelo M et al. Multiplexed ion beam imaging of human breast tumors. Nat. Med. 20, 436–442 (2014). [PubMed: 24584119]

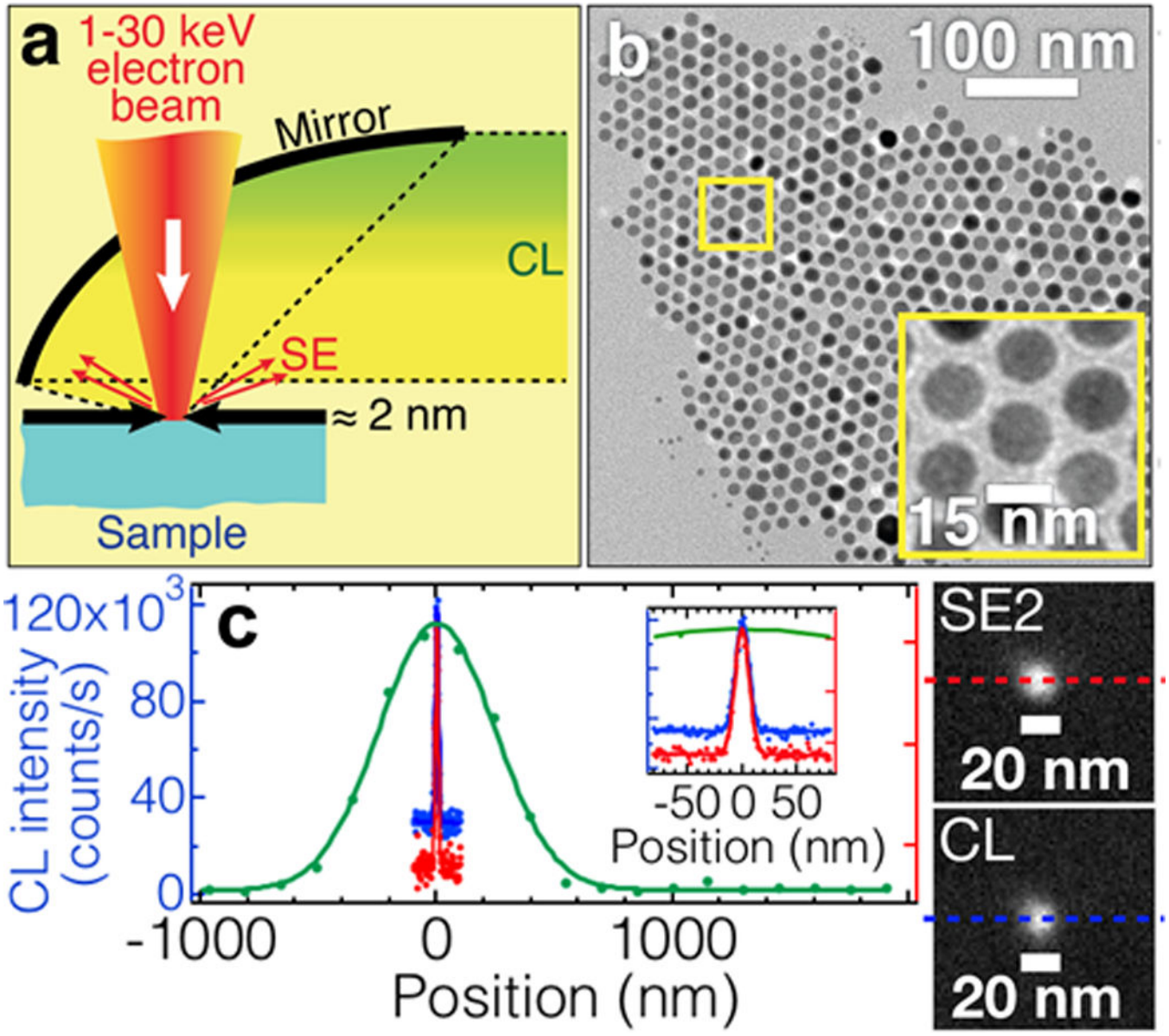

Figure 1. CL microscopy concept.

(a) Illustration of a CL instrument that uses an electron beam to induce emission of photons by nanoparticles shown in (b). CL emission is collected by a parabolic aluminum mirror and focused onto a photon-counting photomultiplier module. (b) TEM of $NaGdF_4$:5% Eu^{3+} nanoparticles. Inset shows a magnified version of a region highlighted with a yellow square. (c) Simultaneous SEM and CL imaging of the particle highlighted with green stars in Fig. 3b. Cross-sectional line profiles of SE electrons (red, right axis) and CL (blue, left axis) scans of a single BF_4^--exchanged $NaGdF_4$:5% Eu^{3+} nanoparticle spin-coated on the Si substrate imaged in parallel. Pixel pitch is 1.95 nm; beam energy is 5 keV; pixel dwell time is 2 ms; beam current is ~400 pA. A cross-sectional line profile of a confocal light microscopy scan of a $NaYF_4$: 18% Yb^{3+}, 2% Er^{3+} nanoparticle of similar size is shown in green (left axis). Excitation wavelength is 980 nm; water immersion objective with 1.27

numerical aperture was used. Inset shows the same data but with zoomed-in *x*-axis. Raw SE and CL data are shown on the right. All cross-sectional line profiles are fit to a single-Gaussian model.

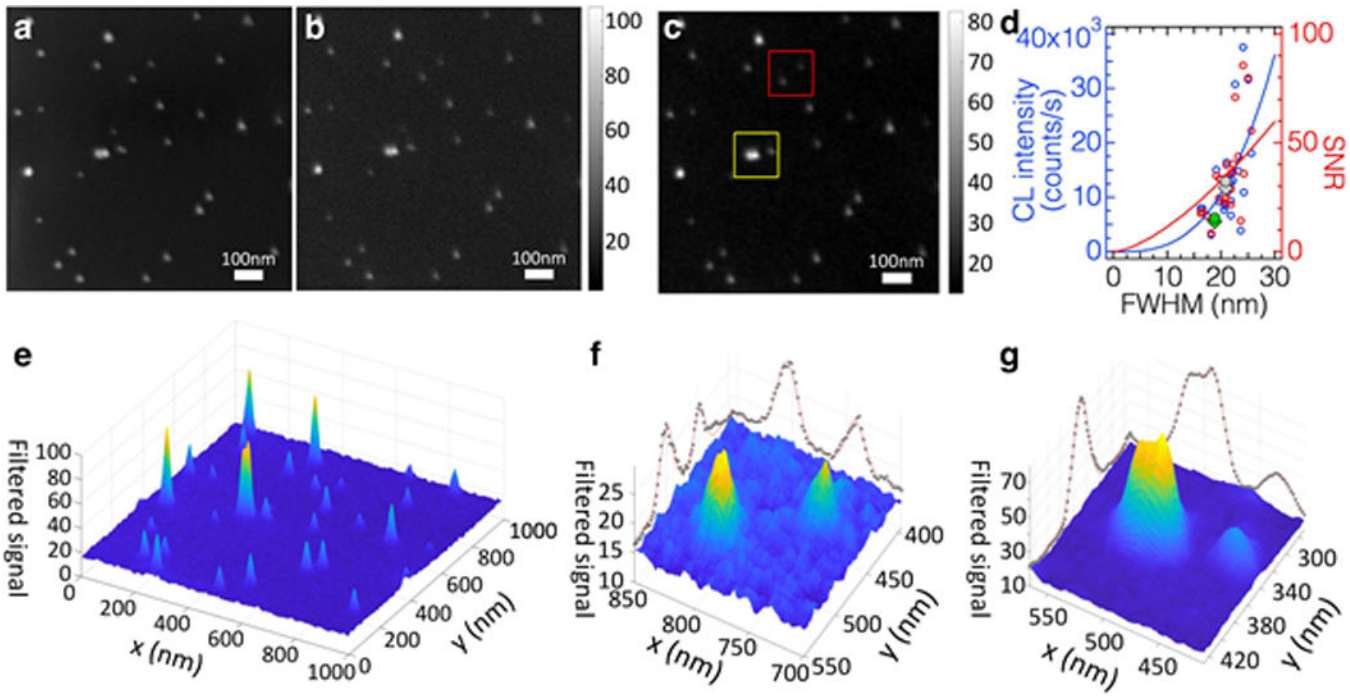

Figure 2. CL imaging of single $NaGdF_4$:5% Eu^{3+}.

The nanoparticles have been BF_4-exchanged and spin-coated on a Si substrate. (a) shows the raw SE image and (b) the corresponding CL signal (detected photons). Images are 1 μm^2; pixel pitch is 1.95 nm; beam energy is 5 keV; pixel dwell time is 2 ms (8 min 44 s image acquisition time); beam current is ~400 pA. (c) depicts the Fourier-filtered CL image of (b) using a Gaussian smoothing function of σ = 7.16 nm. (d) CL intensity (blue, left axis) and CL SNR (red, right axis) for all the single nanoparticles from panels (a, b) are plotted as a function of the nanoparticle SEM full-width-half-maximum (FWHM 2.35σ) of the two-dimensional Gaussian distribution fitted to each nanoparticle CL signal. (Note: The TEM diameter (13.9 ± 5.0 nm) is a more accurate measurement of the particle diameter than SEM, which can be skewed by charging and contamination (See Fig. 1b and Fig. S4 for TEM data)). Panel (e) is a three-dimensional representation of (c). (f, g) show images of the zoomed-in red and yellow regions in panel (c). The data points for the nanoparticles in panel (f) are highlighted with diamonds (CL signal) and circles (CL SNR); Gray corresponds to the brighter and green to the dimmer nanoparticle. A doublet of nanoparticles is shown in panel (g). The dotted points on the sides correspond to a maximum intensity projection of the filtered CL signal. The red lines represent a guide to the eye (Gaussian fit).

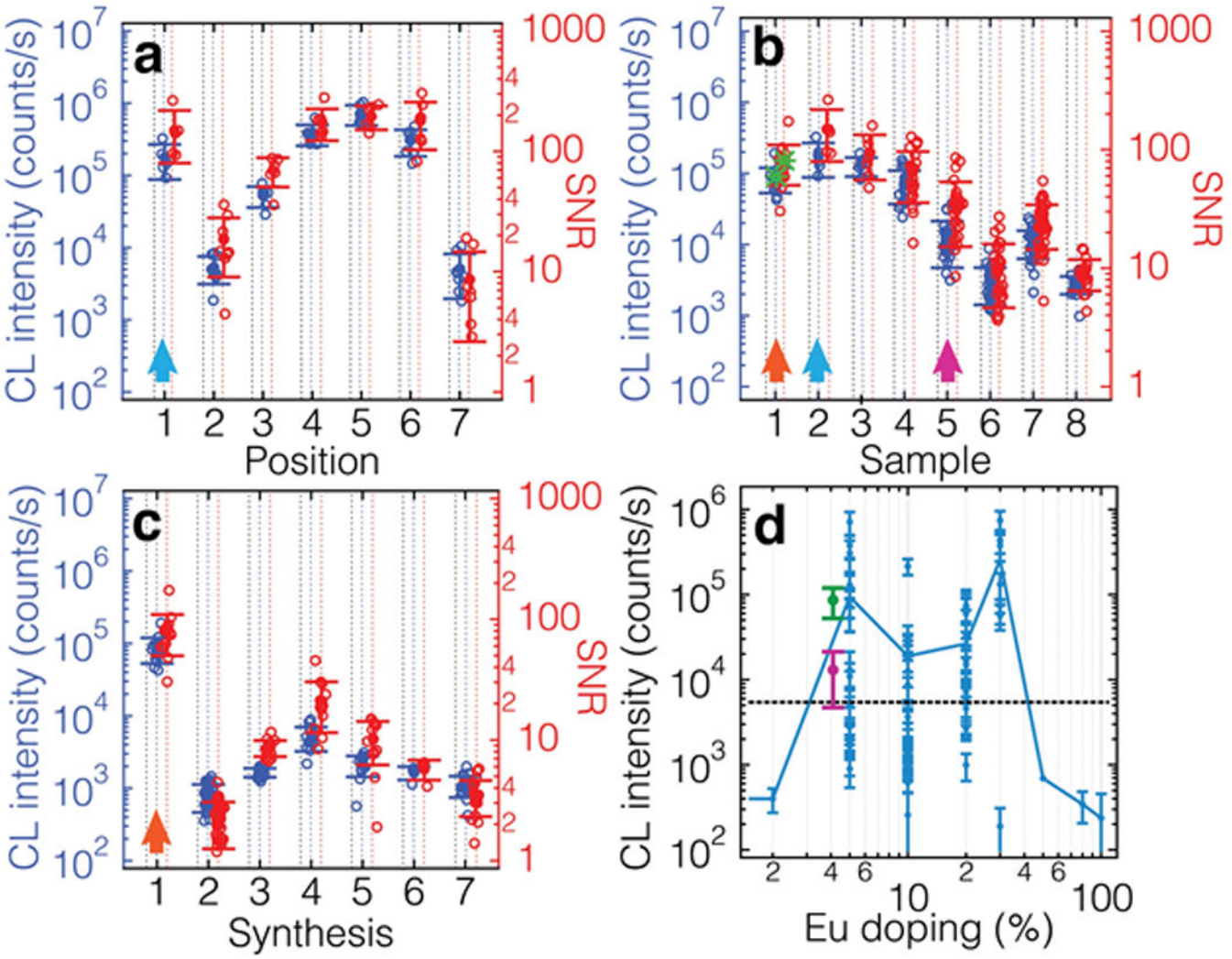

Figure 3. Variability of CL brightness and SNR.

In all experiments $NaGdF_4$:5% Eu^{3+} nanoparticles were BF_4^--exchanged and spin-coated on a Si substrate. CL variability and SNR are shown in (a) for the same sample (Sample #2 in (b)) of the brightest synthesis run (Synthesis #1 in (c)), (b) for synthesis #1 but for different sample preparation, and (c) across different synthesis runs. Identical samples are marked with two blue arrows in (a-b) and two orange arrows in (b-c). Data used in Fig. 1c is highlighted in (b) with green stars and in (d) with a green data point (sample average). Data from Fig. 2 is highlighted with a magenta arrow in (b) and a magenta data point in (d). Empty circles represent the brightness (Gaussian amplitude) in counts per second (blue, y-axis on the left) and the respective CL SNR (red, y-axis on the right) for individual nanoparticles. The filled circles represent the corresponding average values. Panel (d) shows the average single nanoparticle brightness (each point has 1 μm^2 field of view) as a function of Eu^{3+} doping. Green and magenta data points represent data used in Fig. 1c and Fig. 2 (data points are offset to the left for visibility and correspond to 5% Eu^{3+}). The data include all measured samples (incl. different syntheses, different samples but same synthesis, and different regions of the same sample). The solid blue line represents an average of intensities

for each Eu^{3+} doping. The black horizontal dashed line represents the average noise level from panels (a-c) (5449 counts/s) to illustrate the marginal CL intensity. All error bars correspond to one standard deviation.

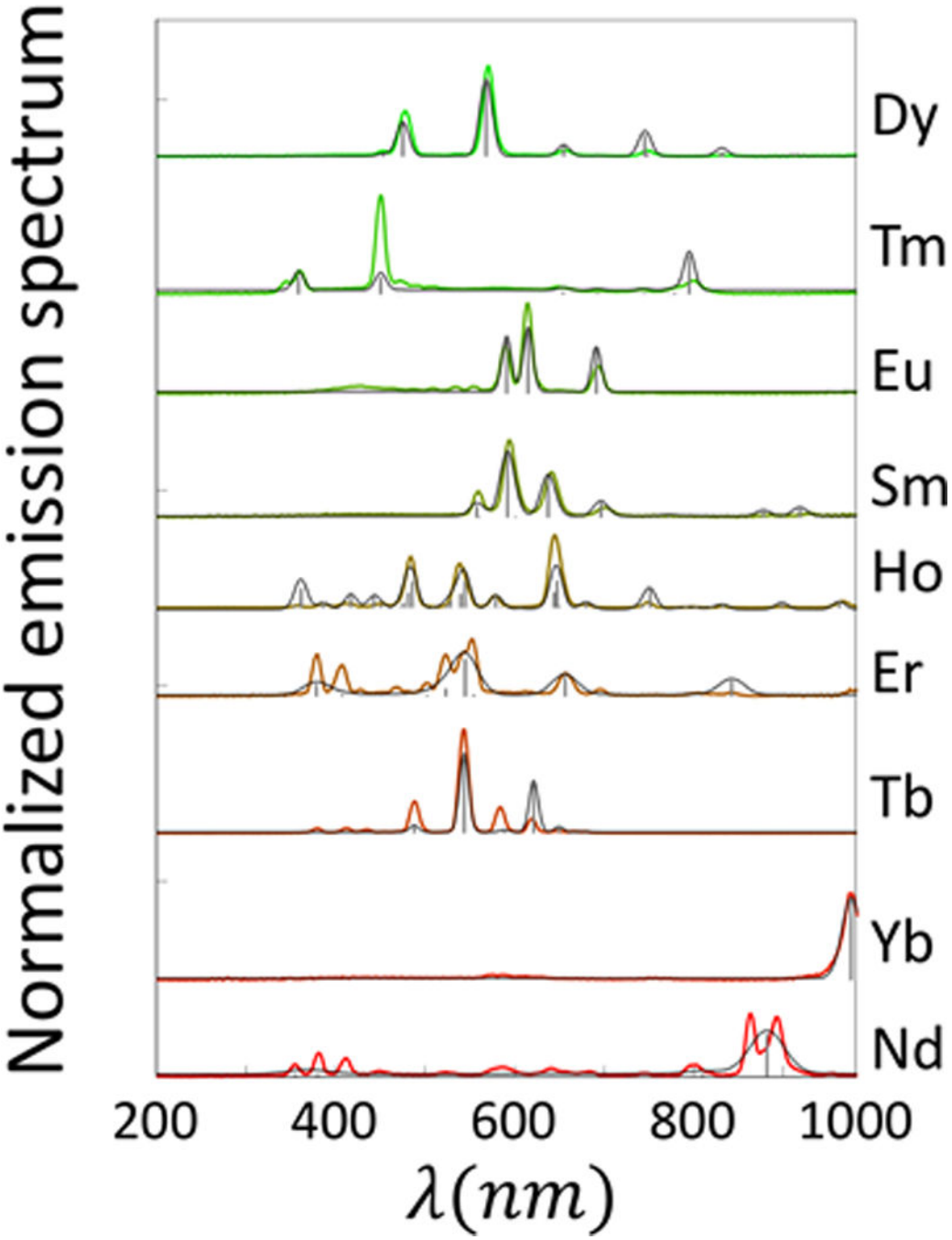

Figure 4. Multicolor imaging of lanthanide-based nanoprobes.

(a) Emission spectra of ensemble samples of *n*-hexane-washed $NaGdF_4$ (solid colored lines) nanoparticles doped with different lanthanide ions (20 % doping for Er^{3+}; 15 % doping for the others) drop-cast on a Si substrate. The data were acquired at 5 keV electron beam energy and corrected for spectrometer efficiency. Gray bars correspond to the Judd-Ofelt calculations (see Methods section “Simulations of nanoparticle spectra” and Fig. S31). The gray lines correspond to fitted spectra using linewidth as the only fitting parameter.